



Stainless steel pitting and early-stage stress corrosion cracking under ultra-low elastic load



Longkui K. Zhu^a, Yu Yan^a, Lijie J. Qiao^{a,*}, Alex A. Volinsky^{b,a}

^a Corrosion and Protection Center, Key Laboratory for Environmental Fracture (MOE), University of Science and Technology Beijing, Beijing 100083, People's Republic of China

^b Department of Mechanical Engineering, University of South Florida, Tampa, FL 33620, USA

ARTICLE INFO

Article history:

Received 28 May 2013

Accepted 29 August 2013

Available online 7 September 2013

Keywords:

A. Stainless steel

B. SEM

B. Modeling studies

C. Stress corrosion

C. Pitting corrosion

C. Anodic dissolution

ABSTRACT

Pitting and crack nucleation at the early stages of stress corrosion cracking (SCC) under ultra-low elastic load were studied. Pits initiated on the sample surface and grew faster in the thickness direction rather than other directions. This corresponds with the stress and strain concentrations calculated using the finite element analysis. At the ultra-low elastic stress levels it is essential for the stress corrosion cracks to emanate from the pits/defects on the sample surface. Furthermore, the preferential SCC initiation sites are at the shoulders, rather than at the bottoms of the surface pits/defects.

© 2013 Elsevier Ltd. All rights reserved.

1. Introduction

The deleterious effect of stress corrosion cracking (SCC) on the mechanical properties of materials is well known in the nuclear power plants, petrochemical and aerospace industries, bridges and ships. Much effort has been dedicated to the mechanisms and predictive approaches of this type of damage. The film rupture model [1,2], corrosion enhanced plasticity model [3–8], and the uniform model of environmentally-assisted cracking [9,10] have been considered, however, successful predictive methods of SCC are still scarce. One of the reasons is that the mechanisms of SCC crack initiation and propagation are possibly altered in the process of crack extension under static loading. In order to address this important issue, our study concentrates on the correlation between pitting and crack nucleation at the early stages of SCC.

During the past decade, a consensus has been reached about SCC cracks originating from pits for smooth samples [11–20]. Generally, when pitting precedes SCC, the fundamental steps in the overall process include: pit initiation, pit growth and transition from pit to crack [12]. The previous view on pit initiation is that pits nucleate stochastically on specimen surfaces [21–23]. However, recent research has shown that the surface stoichiometric inhomogeneities, such as oxide inclusions [24], carbide precipitates [25] and sulphide inclusions [26] in stainless steel (SS), are key factors inducing the preferential pitting initiation. For homoge-

neous materials, Martin et al. [27] showed that 70% of the pits started at strain hardened areas, resulting from mechanical polishing of 304L SS samples in an aqueous chloride-containing solution. The surface strains determine locations of the first pits on the sample surface. Besides, hydrogen can intensify the disorder of passive films, facilitate the drop of the breakdown potential, and finally increase the number of active sites for the pit formation [28–31]. It is emphasized that these active sites usually emerge at the ferrite/austenite interfaces, or inside the ferrite phases in duplex SS [32]. Therefore, the corrosive environment also affects the prior sites of pit initiation. From these points of view, pit initiation, not stochastic, seems to be a deterministic process. For the pit growth, deterministic models, based on the anodic dissolution kinetics, have been developed [33–35]. Two and three-dimensional (3-D) results demonstrated that a pit often formed a lacy metal cover, especially at the early stages of a pit's life [36–38], and tended to become dish-shaped, rather than hemispherical [34]. Nevertheless, on the basis of the autocatalysis theory in the occluded cell, a pit has a higher dissolution rate along the pit depth direction than other directions. Consequently, pit growth is also a controversial issue.

When pits grow to a critical size, they transform into cracks under load. Kondo and Macdonald et al. [14,39,40] proposed that the pit depth was greater than a threshold depth for crack initiation, and the subsequent crack growth rate should exceed the pit growth rate. To accurately predict this transition, a finite element (FE) method has been used to obtain stress and strain fields. Pida-parti et al. [41–43] showed that the stress followed the defect profile, with the maximum stress (below the yield strength) being at

* Corresponding author. Tel.: +86 10 6233 4499; fax : +86 10 6233 2345.

E-mail addresses: lqiao@ustb.edu.cn (L.J. Qiao), volinsky@usf.edu (A.A. Volinsky).

the maximum defect depth for plate specimens. Cerit [44] considered that the maximum stress (below the yield strength) occurred slightly below the pit mouth on cylindrical specimens subjected to torsion. Turnbull and Connolly et al. [18,19,45] pointed out that the stress (higher than the yield strength) concentrated at the pit bottom, but the plastic strain was localized on the pit walls below the pit mouth. Therefore, the stress and strain concentration sites changed with the applied load. Quantitative experimental results of pits and SCC cracks showed that 7% of cracks nucleated at the pit bottom, 50% originated from the shoulder of the pit, and the rest broke the pit shoulder and extended beyond the pit bottom [16]. 3-D X-ray microtomographic images also confirm that most of cracks developed at the pit shoulder for cylindrical specimens stressed to 50–90% of the yield strength [15,19]. Consequently, Turnbull and Connolly et al. [18,19] refer to the pit growth-induced dynamic plastic strain as a possible factor determining the transition from pitting to SCC, when the stress around pits exceeds the yield strength. Moreover, in the mixed load mode, Acuna et al. [46] showed that cracks initiated at the zones of the maximum principle normal stress in the pit. These results were different from the Kondo criteria, and the further research on the transition from pit to crack is needed.

This work aims to study whether a SCC crack emanates from a pit under an ultra-low elastic load and how pit initiation, growth and transition from pit to crack occur on plate sample surfaces. First, early-stage crack and pit morphologies, obtained by different methods, were examined to find relationships between SCC cracks and pits, along with characteristics of pit initiation and growth. Second, a FE method was utilized to determine the effect of the normal stress and strain distribution on pits and SCC cracks. The mechanisms of the initiation and growth of pitting, along with early-stage SCC nucleation under ultra-low elastic load, are also discussed in this paper.

2. Experiments and simulation

2.1. SCC and pitting tests

316L SS single crystals were used in this study with the following chemical composition: C-0.007 wt.%, Cr-17.00 wt.%, Ni-13.49 wt.%, Mo-2.54 wt.%, Mn-0.66 wt.%, Si-0.46 wt.%, P-0.0080 wt.%, S-0.0056 wt.%, Fe-balance. The crystals were produced along the [001] direction and machined into 0.7 mm thick specimens with circle holes 2 mm in diameter. Prior to the experiments, the specimens were annealed at 1050 °C for 30 min in argon, water-quenched, ground with 2000 grit emery paper, electrochemically thinned to about 0.5 mm in solutions containing H_3PO_4 , H_2SO_4 , CrO_3 and $C_2H_6O_2$, degreased with acetone in an ultrasonic cleaner and washed with deionized water. The sample geometry is shown in Fig. 1. After the pretreatment, the samples were placed into a glass container filled with a boiling 45 wt.% $MgCl_2$ solution. An ultra-low nominal stress of 20 MPa, calculated for the narrowest section ($2 \times 0.5 mm^2$) perpendicular to the “2” direction (the tensile direction), was applied to the specimens. All experiments were carried out under an open circuit condition, using a weight-type constant load apparatus equipped with a cooling system, two 316L SS single crystal rods and silica grips.

After the tests, each specimen was ultrasonically cleaned, first in deionized water and then in a 5 wt.% HCl + 2 g/L hexamethylenetetramine mixture. For the cracked specimens, early-stage SCC crack and pit morphologies, on side surfaces perpendicular to the “3” direction (the thickness direction), were observed by scanning electron microscopy (SEM). Then, surface layers were removed by mechanical polishing in order to examine the cracks and the pits inside the samples. Afterwards, the crack and pit morphologies

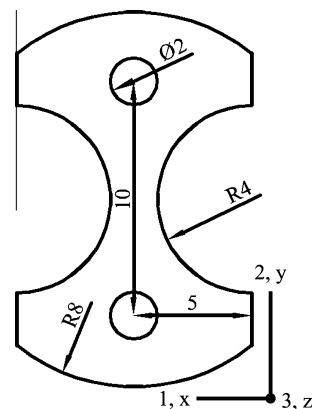


Fig. 1. Schematics of 316L SS single crystal specimens, where the “2, y” direction and the “3, z” directions are the tensile direction and the thickness direction, respectively (dimensions in mm).

on different side surfaces and different cross-sections were compared, and the relationships between the cracking and the pitting were established for the early stage of SCC. Pits and SCC cracks distributed on the plate sample surfaces parallel to the “3” direction were directly observed by SEM.

2.2. Finite element analysis

ABAQUS V6.10-1 was used to investigate the effect of the normal stress and strain on pit initiation, growth and transition to crack under an ultra-low load. To determine the trend of the stress and strain distribution, the simulation was carried out after building 1/8 FE models of specimens with and without a pit, as shown in Fig. 2. The initial pit was embedded into the mid-thickness or the edge of a surface, parallel to the “3” direction, by rotating a $0.02 \times 0.02 mm^2$ (the half length of the axis in the “2” direction \times the half length of the axis in the “3” direction) semicircle and cutting the specimen, as shown in Fig. 2(b) and (c), respectively. For the mid-thickness pit, the half length of the axis in the “3” direction was changed from 0.02 mm to 0.09 mm in 0.01 mm intervals. Since the 1.9 mm diameter 316L SS rod was directly subjected to the applied stress, a quarter of the cylinder model was built with a 1.9 mm diameter and 0.25 mm thickness, and then

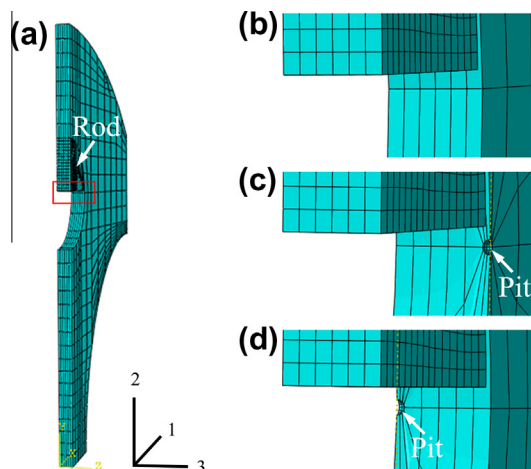


Fig. 2. (a) The 1/8 model of the rod and the specimen without a pit for finite element analysis, (b) mesh structure in the area marked by a box in (a), (c) partial mesh structure of the specimen with a mid-thickness pit in the same area as (b), (d) partial mesh structure of the specimen with an edge pit in the same area as (b).

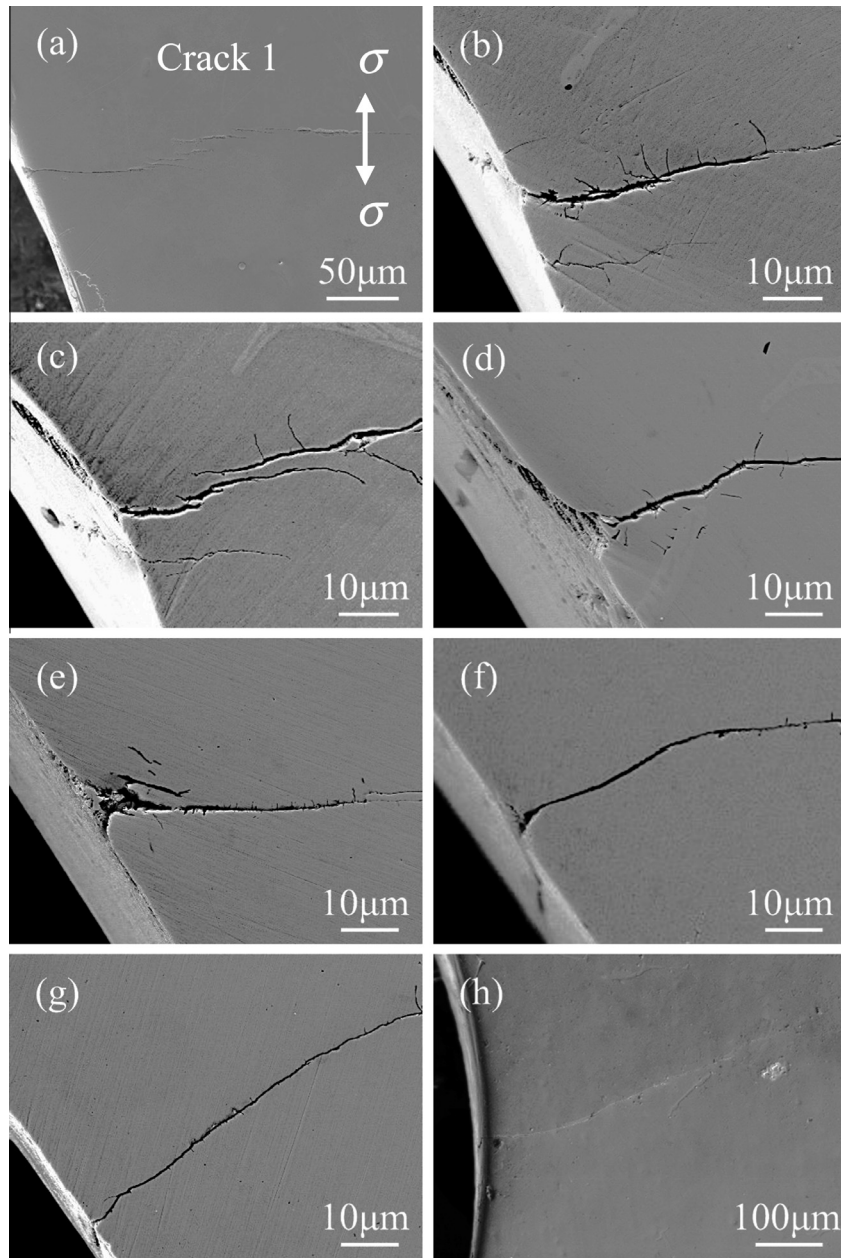


Fig. 3. SEM micrographs of the Crack 1 and the pit on side surfaces and cross-sections (a) 0 μm , (b) 48 μm , (c) 68 μm , (d) 82 μm , (e) 110 μm , (f) 135 μm , (g) 197 μm and (h) 495 μm deeper than the reference surface in (a).

interacted with the specimen by surface-to-surface elastic contact, as shown in Fig. 2. In this model, the mesh was created using the 3-D C3D20 elements (quadratic 20-node elements). The boundary conditions were as follows:

$$\begin{aligned} x = 0, u_x &= 0 \\ y = 0, u_y &= 0 \\ z = 0, u_z &= 0 \end{aligned} \quad (1)$$

To account for the test load, a uniform stress of 21 MPa was applied in the “2” direction. The Young modulus of 188 GPa and Poisson’s ratio of 0.3 for the 316L SS single crystal were the input parameters for the FE model. The normal stress, S_{22} , and the normal strain, LE_{22} , in the “2” direction were used in the analysis to characterize the elastic behavior of the material.

3. Experimental results

3.1. Early-stage SCC crack and pit morphology

SCC cracks primarily nucleated at the leftmost or rightmost edges of the circular holes in Fig. 1. The morphologies of the early-stage Crack 1, Crack 2 and their corresponding pits distributed on different side surfaces and different cross-sections perpendicular to the sample thickness direction, are shown in Figs. 3 and 4. The side surfaces in Figs. 3(a) and 4(a) are defined as the reference planes. Crack 1 was found on each surface, as seen in Fig. 3(a–h). In addition to the crack, the profiles of a pit were also observed in cross-sections 82 μm , 110 μm and 135 μm deeper than the reference plane, as seen in Fig. 3(d–f). The length of the pit was approximately 53 μm along the sample thickness direction

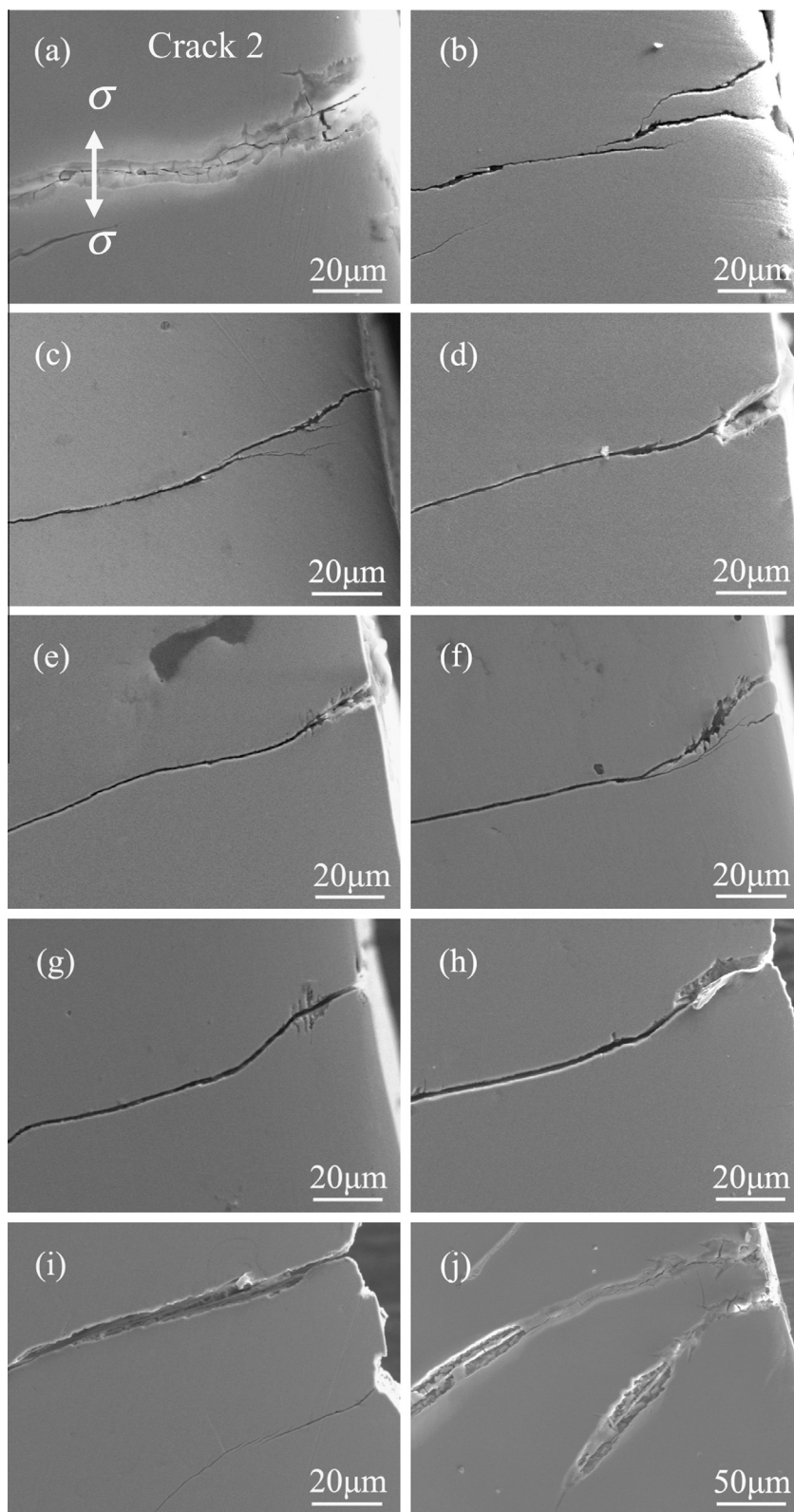


Fig. 4. SEM micrographs of the Crack 2 and the pits on side surfaces and cross-sections (a) 0 μm , (b) 6 μm , (c) 47 μm , (d) 92 μm , (e) 109 μm , (f) 159 μm , (g) 213 μm , (h) 293 μm , (i) 335 μm and (j) 470 μm deeper than the reference surface in (a).

and the maximum pit length in the sample plane direction, i.e., the maximum pit depth, was about 10 μm . In the same way, the individual images of each exposed surface containing Crack 2 are shown in Fig. 4. Two pits are examined in cross-sections 92 μm ,

109 μm and 293 μm deeper than the reference surface, as seen in Fig. 4(d–e) and Fig. 4(h). Similar to Crack 1, Crack 2 passed through the two pits. For the pit in Fig. 4(d–e), the maximum pit depth was about 20 μm along the sample plane direction, and the length was

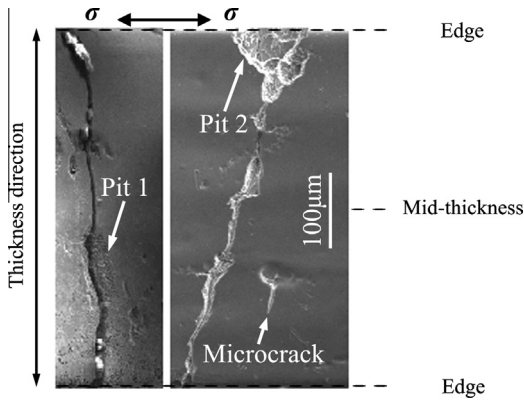


Fig. 5. SEM micrographs of pits, cracks and defects distributed on sample surfaces.

more than 17 μm in the sample thickness direction. As a consequence, the above findings obtained by removing the surface layers reveal that the two cracks passed through their corresponding pits, distributed on the cross-sections tens to hundreds of micrometers deeper than the reference planes, and the length of some pits in the sample thickness direction was larger than the pit depth along the sample plane direction.

Next, early-stage SCC crack and pit morphologies on sample surfaces are shown in Fig. 5. It is found that Pit 1 was located near

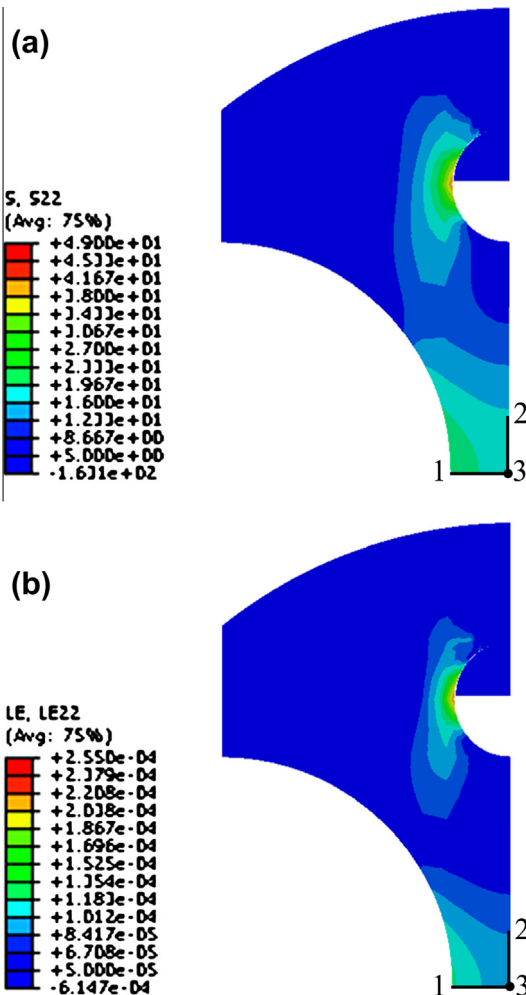


Fig. 6. Distribution of (a) the normal stresses, S_{22} , and (b) the normal strains, LE_{22} , on a side surface of the specimen without a pit.

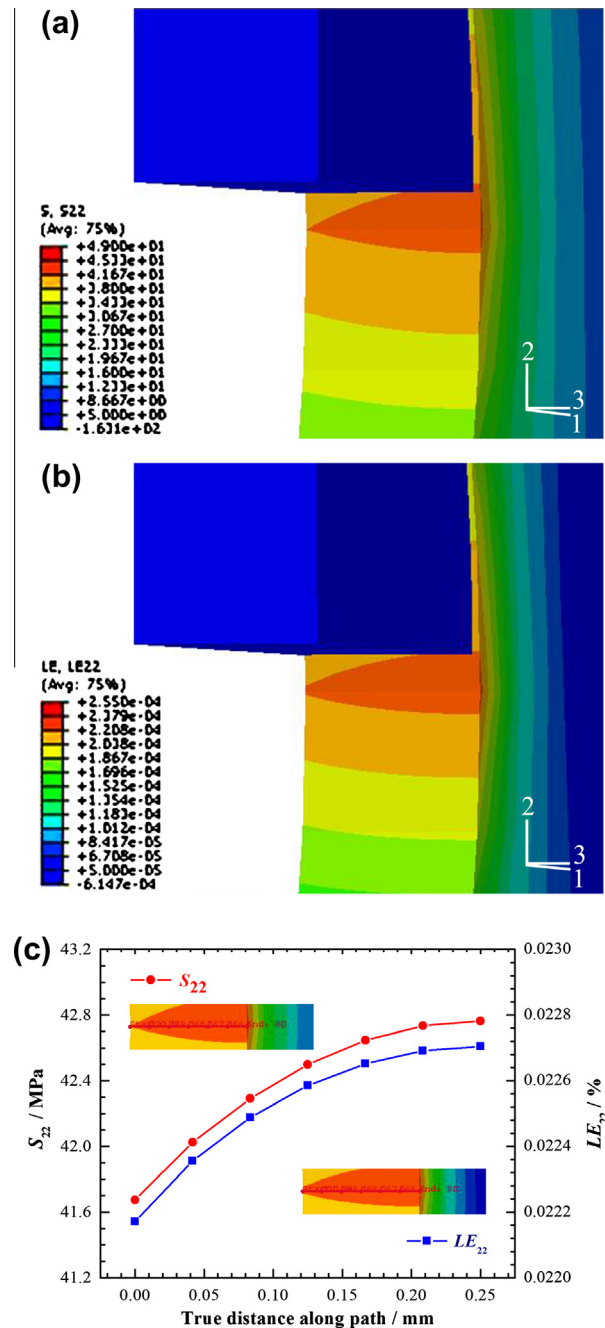


Fig. 7. Distribution of (a) the normal stresses, S_{22} , and (b) the normal strains, LE_{22} , on the arc surface without a pit, (c) S_{22} and LE_{22} distributed along the paths.

the sample mid-thickness, rather than at the edge of the sample. The pit length along the sample thickness direction was larger than that perpendicular to the thickness direction. However, Pit 2 was at the edge, and the length in different directions was almost equal. 23 Pits, from 50 μm to 200 μm in size, were investigated, and 14 of them were asymmetric, with the larger length along the sample thickness direction. Namely, most of the pits grew faster along the sample thickness direction under the ultra-low constant load. Early-stage SCC cracks are also seen in Fig. 5. Two through-thickness cracks separately divided Pit 1 and Pit 2 into two parts, and a microcrack nucleated at the shoulder of a similar pitting defect. Therefore, it is possible for the cracks and the microcrack to emanate from the pits/defects at the early stages of SCC at the ultra-low stress levels.

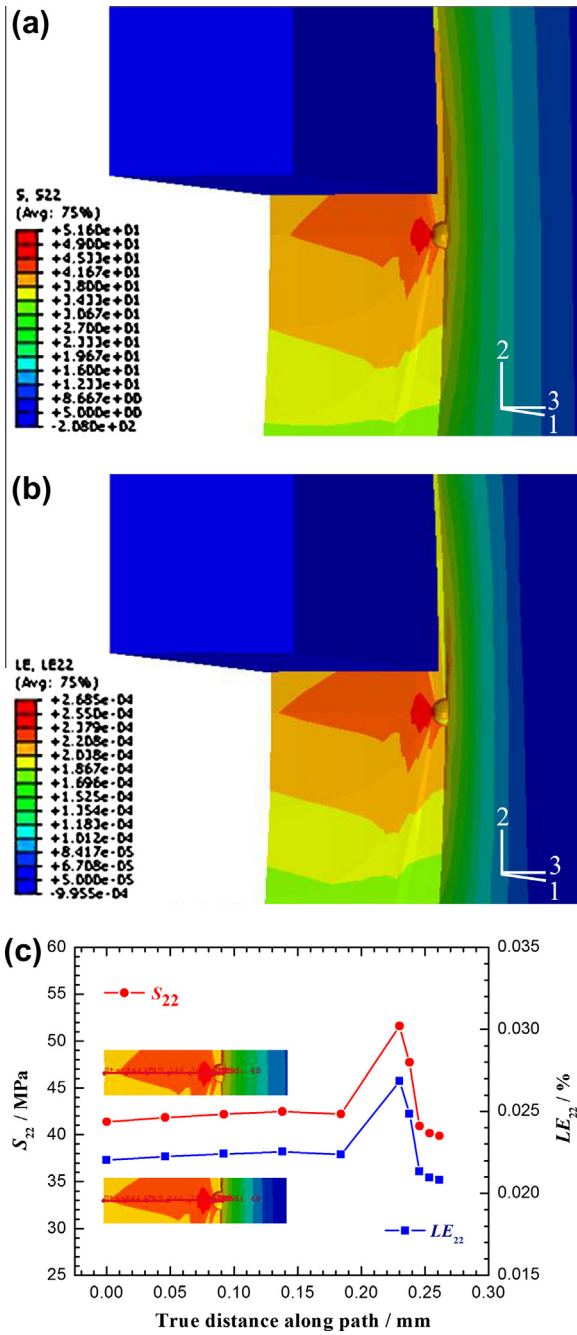


Fig. 8. Distribution of (a) the normal stresses, S_{22} , and (b) the normal strains, LE_{22} , on the arc surface with a mid-thickness pit, (c) S_{22} and LE_{22} distributed along the paths.

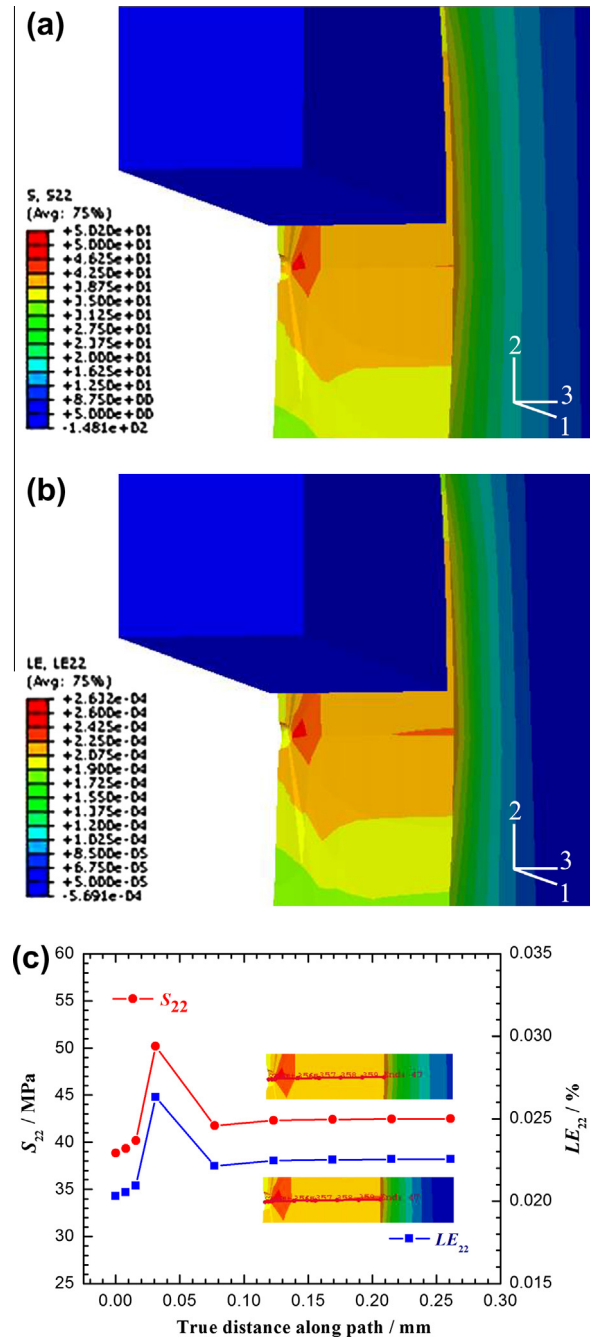


Fig. 9. Distribution of (a) the normal stresses, S_{22} , and (b) the normal strains, LE_{22} , on the arc surface with an edge pit, (c) S_{22} and LE_{22} distributed along the paths.

3.2. Stress and strain distribution

A FE method was used to evaluate the normal stresses, S_{22} , and the normal strains, LE_{22} , distributed on specimens with and without a pit. As seen in Fig. 6(a) and (b), the peak values of S_{22} and LE_{22} simultaneously appeared at the leftmost edge of the semi-circle hole, 41.7 MPa and 0.022%, respectively, which were in the elastic range. However, based on Fig. 7(a) and (b), this kind of the elastic stress and strain concentration was transferred from the leftmost edge to the sample mid-thickness. A path was created from the leftmost edge to the sample mid-thickness in the “3” direction and S_{22} , as well as LE_{22} at the sample mid-thickness were 42.8 MPa and 0.023%, respectively, slightly higher than at the

leftmost edge, as shown in Fig. 7(c). Then, an initial pit was embedded into the mid-thickness or the leftmost edge of the sample, shown in Figs. 8 and 9, respectively. As seen in Figs. 8(a) and (b) and 9(a) and (b), the maximum values of S_{22} and LE_{22} emerged at the pit shoulders, rather than at the bottom of the two pits. The pit shoulder is at the pit mouth, different from the plastic strain concentration zone below the pit mouth due to the cylindrical sample shape [18,19,45]. Calculated numerically, S_{22} and LE_{22} at the shoulder of the mid-thickness pit were 51.6 MPa and 0.027%, respectively, and their corresponding values at the pit bottom were 39.9 MPa and 0.020%, as shown in Fig. 8(c). For the edge pit, S_{22} and LE_{22} at the pit shoulder, were 50.2 MPa and 0.026%, respectively, about 1.3 times larger than those at the pit bottom, as shown in Fig. 9(c). Further, the growth of the mid-thickness pit was

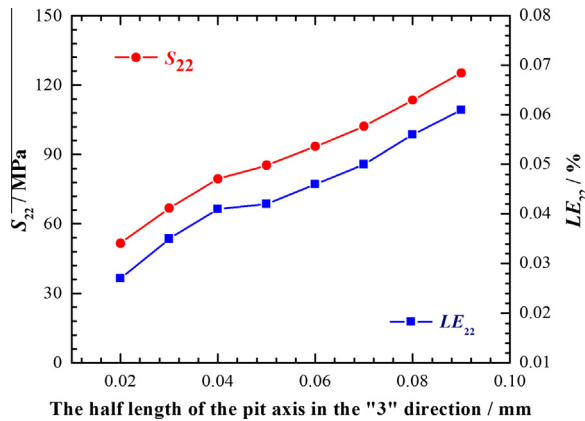


Fig. 10. Variation of the normal stresses, S_{22} , and the normal strains, LE_{22} , at the pit shoulders VS the half length of the mid-thickness pit axis in the "3" direction.

investigated when the applied stress was kept constant. The half length of the semi-ellipse axis in the "3" direction was changed from 0.02 mm to 0.09 mm with 0.01 mm intervals. The results in Fig. 10 indicate that S_{22} and LE_{22} at the pit shoulder gradually increased in the process of pit growth, and the maximum values of S_{22} increased to 125.2 MPa from 51.6 MPa, while LE_{22} increased to 0.061% from 0.027%. The maximum stresses and strains were in the elastic range, known from the pit-growth induced plasticity [18,19,45].

4. Discussion

4.1. Pit initiation and growth

Pit initiation and growth is essentially an electrochemical process. For pit initiation, stochastic and deterministic models have been proposed during the past decades. Experimental results show that the pits nucleated near the mid-thickness and at the edges of the plate sample surfaces parallel to the thickness direction under the ultra-low elastic loading. In general, the distinction of specimen surface features, such as stoichiometric inhomogeneity, different stresses or strains and the corrosive environment are capable of inducing the nucleation of pitting as a result of the surface potential fluctuations [25–27,32]. The stress potential (E_{22}) and the strain potential (V_{22}) are proportional to the stress (S_{22}) and the strain (LE_{22}), respectively [47]:

$$E_{22}^2 \propto S_{22}^2 \quad (2)$$

$$V_{22}^2 \propto LE_{22}^2 \quad (3)$$

FE analysis indicates that both the normal stress and strain at the mid-thickness, 42.8 MPa and 0.023%, were slightly higher than at the edge, 41.7 MPa and 0.022%. According to Eqs. (2) and (3), this kind of stress and strain concentration in the elastic range is able to cause a small variation in the surface potential, less than 5%. Perhaps, the tiny potential difference is not sufficient for pit initiation. However, there is no absolute smooth geometric surface and the surface fluctuations exist in all materials, including electrochemically thinned 316L SS single crystal specimens. Since the stresses were not uniformly distributed on rough surfaces [48], it is likely that the local stress or strain concentration at the surfaces provides beneficial conditions for the formation of negative potential sites. On the other hand, hydrogen and passive films significantly affect pitting [28–31]. The local activation of the surfaces also takes place due to hydrogen absorption and adsorption combined with passive film rupture. Once the potential at an active site is equal to the pit

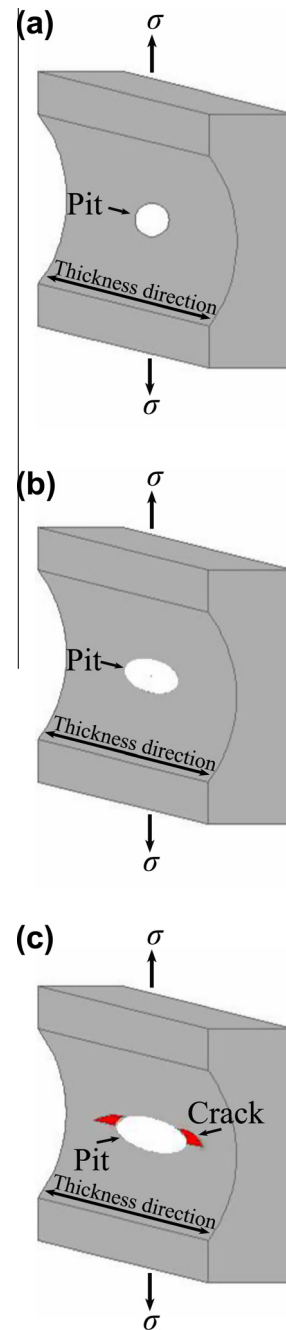


Fig. 11. The whole process of pitting and early-stage SCC initiation on a surface parallel to the thickness direction under an ultra-low load: (a) a pit nucleus forms at the mid-thickness of the surface parallel to the thickness direction, (b) the pit grows fast along the thickness direction, which leads to the formation of the long pit, and (c) SCC cracks preferentially initiate at two pit shoulders.

potential, E_p , a pit nucleus can be produced in a boiling 45 wt.% $MgCl_2$ solution. It is considered that the coupling effect of the macroscopic stress and strain concentration together with the local activation is a crucial reason determining the pits nucleation near the mid-thickness and at the edges of the plate sample surfaces.

From the starting point, an unstable pit often grows by active metal dissolution within the pit [33–37,43,46]. The anodic reaction is represented by:



where n is the average charge on the dissolved metal ions. For 316L SS single crystals, the dissolution products are Fe^{2+} , Ni^{2+} and Cr^{3+} .

On the basis of the autocatalysis theory in the occluded cell, a pit has a higher dissolution rate along the pit depth direction than other directions. Ernst and Davenport et al. [36–38] considered that a pit often formed a lacy metal cover, especially at the early stages of a pit's life, and tended to become dish-shaped. Nevertheless, experimental results show that the majority of the pits grew fast along the sample thickness direction at the ultra-low stress levels, leading to the formation of the semiellipsoid-shaped pits. Both the maximum normal stress and strain appeared at the shoulders and were about 1.3 times larger than those at the bottoms of the mid-thickness pit and the edge pit. Perhaps, the stress and strain distribution causes the prior pit growth location transfer from the pit bottom to the pit shoulder by varying the surface potential distribution. In the light of Eqs. (2) and (3), the potential at the pit shoulder becomes 23% lower than that at the pit bottom and the anodic dissolution with a high rate occurs at the pit shoulder. In this process, the normal stress and strain gradually increase around the pit shoulder, promoting pit growth in the thickness direction. In the end, the semiellipsoid-shaped pit forms with the larger length along the sample thickness direction than the other directions under the constant loading condition.

4.2. The initiation of early-stage SCC under ultra-low elastic load

Generally, a SCC crack often stems from a pit/defect on a specimen surface. The early-stage SCC crack and pit morphologies obtained by different methods demonstrate that the stress corrosion cracks were related with their corresponding pits on the surfaces parallel to the sample thickness direction at the ultra-low stress levels. The cracks extended beyond the pit bottoms and broke the pit shoulders. Additionally, it is also found that the microcrack started from the shoulder of the similar pitting defect. These cracks are likely to emanate from the pits/defects. According to the Kondo criteria, the SCC initiation occurred when the pit depth was greater than a threshold depth [14,39,40]. Connolly et al. [19] considered that the threshold pit depth was approximately 150–200 μm for the applied stress of about 50% $\sigma_{0.2}$. In the experiment, the applied stress was lower than 50% $\sigma_{0.2}$. In theory, the threshold pit depth should be larger at the stress level for SCC initiation. In fact, the pit depth was only dozens of micrometers under the ultra-low elastic load. As a result, the pit depth is not the deterministic factor causing the early-stage SCC initiation. Turnbull and Connolly et al. [18,19] referred to the pit growth-induced dynamic plastic strain as a possible factor determining the transition from pitting to SCC, when the stress around pits exceeded the yield strength. In this work, the FE analysis indicates that the stress and strain are linear under the ultra-low elastic load. From the stress point, a SCC crack is capable of nucleating when the local stress, σ_1 , is equal to or greater than a critical value, σ_{ISCC} :

$$\sigma_1 \geq \sigma_{\text{ISCC}} \quad (5)$$

Alyousif and Nishimura [49] systematically investigated the effect of the applied stress on SCC of austenitic SS in boiling MgCl_2 solutions, finding that σ_{ISCC} was in the 100–200 MPa range. Simulation results of this paper show that there was the stress and strain concentration on the plate sample surface without the pit and the maximum normal stress was 42.8 MPa at the mid-thickness. At this stress level, the SCC crack nucleation event is difficult to occur. However, when the pit was embedded into the surface parallel to the sample thickness direction, the peak value could be up to 125.2 MPa, almost equal to σ_{ISCC} . The pit length was 0.18 mm along the sample thickness direction, matching the experimental observation of about 0.1 mm. Consequently, it is necessary for the cracks and the microcrack to originate from the pits/defects at the early stages of SCC under the ultra-low elastic load.

Which sites of the pits/defects do the early-stage SCC cracks start from? In this study, the through cracks divided the pits into two parts, while the microcrack initiated at the defect shoulder, rather than at the defect bottom. This phenomenon coincides with the finding that most of the SCC cracks nucleated near the pit shoulder [15,18,19]. Further, the FE analysis indicates that both the normal stress and strain simultaneously concentrated at the pit shoulder, not at the pit bottom. As a result, the shoulders of the pits/defects should be the preferential initiation sites of the cracks and the microcrack at the early stages of SCC. Besides, it is possible for some cracks to start at the pit/defect bottom. Since the normal stress was low at the pit bottom, it is considered that the localized variation in solution chemistry may play a critical role in the nucleation of these cracks.

In short, on the plate specimen surfaces without the defects, pitting precedes SCC at the ultra-low stress levels. The whole process is described as follows: Under an ultra-low load, macroscopic stress and strain concentration together with local activation induces a pit to initiate near the mid-thickness, or at the edge of a surface parallel to the sample thickness direction. The mid-thickness pit is shown in Fig. 11(a). Once the pit nucleus forms, both concentration points of the normal stress and the normal strain transfer to the pit shoulder. This produces a high anodic dissolution rate at the pit shoulder and leads to the formation of the pit with the large length along the sample thickness direction in Fig. 11(b). Then, with the pit enlarging, the normal stress and strain gradually increase at the pit shoulders. When the local stress is equal to or greater than σ_{ISCC} , an early-stage SCC crack can emanate from the pit. The preferential SCC nucleation site is the pit shoulder, as shown in Fig. 11(c). In the industry, pits also first form and then SCC cracks initiate from the pits/defects due to the low allowable stress. As a consequence, the prevention of pitting is the first step to prolong service life at the low stress levels. The limitation of the research is that a few chemical factors, such as pH, are not considered, and the effect of the high load on the transition from pit to crack needs to be investigated.

5. Conclusions

- (1) The FE analysis shows that the normal stress and strain at the sample mid-thickness were slightly higher than at the edge of the plate sample surface without the pit. When the pit was embedded into the mid-thickness, or the edge of the sample surface, both the normal stress and strain concentration appeared at the shoulder of the mid-thickness pit, or the edge pit. Keeping the applied stress constant, it was also found that the normal stress and strain at the pit shoulder gradually increased with the larger pit.
- (2) The pits initiated near the mid-thickness and at the edges of the sample surfaces parallel to the thickness direction, which was possibly induced by the coupling effect of the macroscopic stress and strain concentration together with the local activation.
- (3) The length of most pits was larger along the thickness direction than other directions. The phenomenon may result from the normal stress and strain concentration at the pit shoulders.
- (4) The early-stage SCC cracks were related with their corresponding pits/defects. On account of the ultra-low applied stress, it is necessary for the SCC cracks to emanate from the pits/defects on the plate specimen surfaces parallel to the sample thickness direction. In addition, the preferential nucleation event should occur at the shoulders, and not at the bottom of the pits/defects.

Acknowledgments

This work was supported by the National Nature Science Foundation of China (50731003 and 51171024). AV would like to acknowledge support from the National Science Foundation.

References

- [1] H.L. Logan, Film-rupture mechanism of stress corrosion, *J. Res. Natl. Bur. Stand.* 48 (1952) 99–105.
- [2] R.C. Newman, C. Healey, Stability, validity and sensitivity to input parameters of the slip-dissolution model for stress-corrosion cracking, *Corros. Sci.* 49 (2007) 4040–4050.
- [3] L.J. Qiao, K.W. Gao, A.A. Volinsky, X.Y. Li, Discontinuous surface cracks during stress corrosion cracking of stainless steel single crystal, *Corros. Sci.* 53 (2011) 3509–3514.
- [4] J.X. Li, W.Y. Chu, Y.B. Wang, L.J. Qiao, In situ TEM study of stress corrosion cracking of austenitic stainless steel, *Corros. Sci.* 45 (2003) 1355–1365.
- [5] W.F. Flanagan, P. Bastias, B.D. Lichter, A theory of transgranular stress-corrosion cracking, *Acta Metall. Mater.* 39 (1991) 695–705.
- [6] T. Magnin, A. Chambreuil, B. Bayle, The corrosion-enhanced plasticity model for stress corrosion cracking in ductile fcc alloys, *Acta Mater.* 44 (1996) 1457–1470.
- [7] J.P. Chateau, D. Delafosse, T. Magnin, Numerical simulations of hydrogen-dislocation interactions in fcc stainless steels: Part I: hydrogen-dislocation interactions in bulk crystals, *Acta Mater.* 50 (2002) 1507–1522.
- [8] J.P. Chateau, D. Delafosse, T. Magnin, Numerical simulations of hydrogen-dislocation interactions in fcc stainless steels: Part II: hydrogen effects on crack tip plasticity at a stress corrosion crack, *Acta Mater.* 50 (2002) 1523–1538.
- [9] H.W. Liu, A uniformed model of environment-assisted cracking, *Acta Mater.* 56 (2008) 4339–4348.
- [10] H.W. Liu, Reply to comments on “A uniformed model of environment assisted cracking”, *Scripta Mater.* 61 (2009) 335–337.
- [11] H. Inoue, H. Iwakawa, K. Yamakawa, Potential fluctuation during early stage of stress corrosion cracking of type-304 stainless steel in chloride solution, *Mater. Sci. Eng. A* 198 (1995) 225–230.
- [12] A. Turnbull, S. Zhou, Pit to crack transition in stress corrosion cracking of a steam turbine disc steel, *Corros. Sci.* 46 (2004) 1239–1264.
- [13] B.T. Lu, Z.K. Chen, J.L. Luo, B.M. Patchett, Z.H. Xu, Pitting and stress corrosion cracking behavior in welded austenitic stainless steel, *Electrochim. Acta* 50 (2005) 1391–1403.
- [14] A. Turnbull, L.N. McCartney, S. Zhou, A model to predict the evolution of pitting corrosion and the pit-to-crack transition incorporating statistically distributed input parameters, *Corros. Sci.* 48 (2006) 2084–2105.
- [15] B.J. Connolly, D.A. Horner, S.J. Fox, A.J. Davenport, C. Padovani, S. Zhou, A. Turnbull, M. Preuss, N.P. Stevens, T.J. Marrow, J.-Y. Buffiere, E. Boller, A. Groso, M. Stamparoni, X-ray microtomography studies of localized corrosion and transitions to stress corrosion cracking, *Mater. Sci. Technol.* 22 (2006) 1076–1085.
- [16] A. Turnbull, L.N. McCartney, S. Zhou, Modelling of the evolution of stress corrosion cracks from corrosion pits, *Scripta Mater.* 54 (2006) 575–578.
- [17] H. Masuda, SKFM observation of SCC on SUS304 stainless steel, *Corros. Sci.* 49 (2007) 120–129.
- [18] A. Turnbull, L. Wright, L. Crocker, New insight into the pit-to-crack transition from finite element analysis of the stress and strain distribution around a corrosion pit, *Corros. Sci.* 52 (2010) 1492–1498.
- [19] D.A. Horner, B.J. Connolly, S. Zhou, L. Crocker, A. Turnbull, Novel images of the evolution of stress corrosion cracks from corrosion pits, *Corros. Sci.* 53 (2011) 3466–3485.
- [20] A. Turnbull, K. Mingard, J.D. Lord, B. Roebuck, D.R. Tice, K.J. Mottershead, N.D. Fairweather, A.K. Bradbury, Sensitivity of stress corrosion cracking of stainless steel to surface machining and grinding procedure, *Corros. Sci.* 53 (2011) 3398–3415.
- [21] B. Wu, J.R. Scully, J.L. Hudson, A.S. Mikhailov, Cooperative stochastic behaviors in localized corrosion I: model, *J. Electrochem. Soc.* 144 (1997) 1614–1620.
- [22] D.E. Williams, C. Westcott, M. Fleischmann, Stochastic models of pitting corrosion of stainless steels I: modeling of the initiation and growth of pits at constant potential, *J. Electrochem. Soc.* 132 (1985) 1796–1804.
- [23] Z. Szklarska-Smialowska, J. Gust, The initiation of stress corrosion cracks and pits in austenitic Cr–Ni steel in MgCl₂ solutions at 40–90 °C, *Corros. Sci.* 19 (1979) 753–765.
- [24] M.A. Baker, J.E. Castle, The initiation of pitting corrosion of stainless steels at oxide inclusions, *Corros. Sci.* 33 (1992) 1295–1303.
- [25] R.E. Williford, C.F. Windisch Jr, R.H. Jones, In situ observations of the early stages of localized corrosion in type 304 SS using the electrochemical atomic force microscope, *Mater. Sci. Eng. A* 288 (2000) 54–60.
- [26] B. Vuillemin, X. Philippe, R. Oltra, V. Vignol, L. Coudreuse, L.C. Dufour, E. Finot, SVET, AFM and AES study of pitting corrosion initiated on MnS inclusions by microinjection, *Corros. Sci.* 45 (2003) 1143–1159.
- [27] F.A. Martin, C. Bataillon, J. Cousty, In situ AFM detection of pit onset location on a 304L stainless steel, *Corros. Sci.* 50 (2008) 84–92.
- [28] M.E. Armacanqui, R.A. Oriani, Effect of hydrogen on the pitting resistance of passivating film on nickel in chloride-containing solution, *Corrosion* 44 (1988) 696–699.
- [29] Q. Yang, L.J. Qiao, S. Chiovelli, J.L. Luo, Effects of hydrogen on pitting susceptibility of type 310 stainless steel, *Corrosion* 54 (1998) 628–634.
- [30] Q. Yang, L.J. Qiao, Effects of hydrogen on disorder of passive films and pitting susceptibility of type 310 stainless steel, *J. Electrochem. Soc.* 148 (2001) B29–B35.
- [31] J.G. Yu, J.L. Luo, P.R. Norton, Investigation of hydrogen induced pitting active sites, *Electrochim. Acta* 47 (2002) 4019–4025.
- [32] M. Li, L.Q. Guo, L.J. Qiao, Y. Bai, The mechanism of hydrogen-induced pitting corrosion in duplex stainless steel studied by SKPFM, *Corros. Sci.* 60 (2012) 76–81.
- [33] B. Baroux, The kinetics of pit generation on stainless steels, *Corros. Sci.* 28 (1988) 969–986.
- [34] N.J. Laycock, S.P. White, Computer simulation of single pit propagation in stainless steel under potentiostatic control, *J. Electrochem. Soc.* 148 (2001) B264–B275.
- [35] N.J. Laycock, J.S. Noh, S.P. White, D.P. Krouse, Computer simulation of pitting potential measurements, *Corros. Sci.* 47 (2005) 3140–3177.
- [36] P. Ernst, R.C. Newman, Pit growth studies in stainless steel foils: I. Introduction and pit growth kinetics, *Corros. Sci.* 44 (2002) 927–941.
- [37] P. Ernst, R.C. Newman, Pit growth studies in stainless steel foils: II. Effect of temperature, chloride concentration and sulphate addition, *Corros. Sci.* 44 (2002) 943–954.
- [38] S.M. Ghahari, A.J. Davenport, T. Rayment, T. Suter, J.-P. Tinnes, C. Padovani, J.A. Hammons, M. Stamparoni, F. Marone, R. Mokso, In situ synchrotron X-ray micro-tomography study of pitting corrosion in stainless steel, *Corros. Sci.* 53 (2011) 2684–2687.
- [39] Y. Kondo, Prediction of fatigue crack initiation life based on pit growth, *Corrosion* 45 (1989) 7–11.
- [40] G. Engelhardt, D.D. Macdonald, Unification of the deterministic and statistical approaches for predicting localized corrosion damage. I. Theoretical foundation, *Corros. Sci.* 46 (2004) 2755–2780.
- [41] R.M. Pidaparti, R.R. Patel, Correlation between corrosion pits and stresses in Al alloys, *Mater. Lett.* 62 (2008) 4497–4499.
- [42] R.M. Pidaparti, K. Koombua, A.S. Rao, Corrosion pit induced stresses prediction from SEM and finite element analysis, *Int. J. Comput. Methods Eng. Sci. Mech.* 10 (2009) 117–123.
- [43] R.M. Pidaparti, R.K. Patel, Investigation of a single pit/defect evolution during the corrosion process, *Corros. Sci.* 52 (2010) 3150–3153.
- [44] M. Cerit, Numerical investigation on torsional stress concentration factor at the semielliptical corrosion pit, *Corros. Sci.* 67 (2013) 225–232.
- [45] A. Turnbull, D.A. Horner, B.J. Connolly, Challenges in modelling the evolution of stress corrosion cracks from pits, *Eng. Fract. Mech.* 76 (2009) 633–640.
- [46] N. Acuna, J. Gonzalez-Sanchez, G. Ku-Basulto, L. Dominguez, Analysis of the stress intensity factor around corrosion pits developed on structures subjected to mixed loading, *Scripta Mater.* 55 (2006) 363–366.
- [47] J. Weertman, Stress and strain potentials for mode I and mode II cracks, *Mech. Mater.* 37 (2005) 543–550.
- [48] R.M. Pidaparti, A.S. Rao, Analysis of pits induced stresses due to metal corrosion, *Corros. Sci.* 50 (2008) 1932–1938.
- [49] O.M. Alyousif, R. Nishimura, On the stress corrosion cracking and hydrogen embrittlement of sensitized austenitic stainless steels in boiling saturated magnesium chloride solutions: effect of applied stress, *Corros. Sci.* 50 (2008) 2919–2926.